Contribution From Ising Domains Overlapping Out-of-Plane to Perpendicular Magnetic Anisotropy in Mn_4N Thin Films on MgO(001)

Andrew Foley[a], Joseph Corbett[a], Khan Alam[a], Andrea L. Richard[a], David C. Ingram[a], Arthur R. Smith[a,*], Lianshui Zhao[b], James C. Gallagher[b], Fengyuan Yang[b]

[a] *Nanoscale and Quantum Phenomena Institute, Department of Physics and Astronomy, Ohio University, Athens, OH 45701, USA*
[b] *The Ohio State University, Department of Physics, 191 Woodruff Ave., Columbus, OH 43210, USA*

Abstract

Single phase ε-Mn_4N thin and ultrathin films are grown on MgO(001) using molecular beam epitaxy. Reflection high-energy electron diffraction and *out-of-plane* x-ray diffraction measurements are taken for each sample in order to determine the *in-* and *out-of-plane* strain for each sample. Vibrating sample magnetometry and superconducting quantum interference device measurements, which are performed on the thin and ultrathin films respectively, are used to plot the magnetization of each sample versus both *in-* and *out-of-plane* $\vec{\mathbf{H}}$-fields and to determine the magnitude of perpendicular magnetic anisotropy in these films. Three significant components of perpendicular magnetic anisotropy are observed in these films and are attributed to sample strain (1 component) and shape (2 components). Among these components, the most significant component (0.8 to 4.9 $\frac{Merg}{cm^3}$) is identified as a second term of shape anisotropy, which possesses a negative linear relationship with sample thickness over the range from 9 nm to 310 nm. Atomic (magnetic) force microscopy measurements show the presence of a surface localized magnetic polarization (22% to 82%), which increases with decreasing thickness, when the net magnetization of the films is zero. The second term of shape anisotropy as well as the surface localized polarization, which each depend on sample thickness, are each regarded as a consequence of Ising domains overlapping *out-of-plane* in these films.

Keywords: Manganese anti-perovskite, Magnetic force microscopy, Molecular beam epitaxy, Perpendicular magnetic anisotropy
PACS: 68.37.Rt, 75.30.Gw, 75.50.Gg, 75.70.Ak

*Corresponding Author
Email address: smitha2@ohio.edu (Arthur R. Smith)

1. Introduction

Manganese anti-perovskites [Mn_3AX (A: transition metal or semiconducting element, X: N or C)] have shown a wide range of magnetic properties including spin-glass behavior, piezomagnetic effect, giant magnetoresistance, and magnetocaloric effect.[1, 2, 3, 4] In particular, the Mn_3AX material ε-Mn_4N exhibits potential applications in dilute magnetic semiconductors, spin-injection contacts, magnetoresistive devices, microwave shielding, electrochemical capacitors, the synthesis of water-purifying catalysts and as a Cu diffusion barrier in silicon chip manufacturing.[5, 6, 7, 8, 9, 10, 11] This wide range of applications is supported by the many practical aspects of the material. These aspects of ε-Mn_4N include a high Néel temperature (T_N = 738 K) and temperature/chemical stability as well as suitability for growth on a myriad of substrates, such as technologically relevant semiconductors (Si and GaN) and metals (Cu and Al).[12, 13, 14, 15, 16, 17, 18, 19, 20, 21] One property of ε-Mn_4N [perpendicular magnetic anisotropy (PMA)] can be linked with three of the applications of ε-Mn_4N (spin-injection contacts, magnetoresistive devices, and microwave shielding).[7, 22, 23, 24]

Initial studies into ε-Mn_4N PMA by Ching *et al.* indicate that grain size and strain both affect PMA.[15, 16, 17] Since then, multiple studies arguing that the strain term is the primary component of PMA in ε-Mn_4N have been put forward.[7, 19, 24, 25, 29] This is supported by the experimental and theoretical evidence that lattice distortions and temperature changes mediate transitions among many different types of magnetism (non-magnetic, multiple antiferromagnetic/ferrimagnetic orderings, and even mixtures of these types) in ε-Mn_4N.[8, 14, 26, 27, 28, 29, 30, 31] This evidence indicates that strain has a significant role in the magnetic properties of ε-Mn_4N.

On the other hand, an association between columnar grain structure and PMA in ε-Mn_4N is found by Ching *et al.*[17] In addition, measurements from Yuping *et al.* demonstrate a strong dependence of magnetic permeability and microwave absorption on ε-Mn_4N grain size.[23] Together these two studies suggest that grain size, and therefore shape anisotropy, in addition to strain play an important role in the magnetic properties of ε-Mn_4N. For this reason, additional study of the effect of shape anisotropy on PMA in ε-Mn_4N while taking care to consider the effect of strain is of particular interest.

In this study, Mn_4N thin films of varying thickness (t = 9 to 310 nm) and tetragonal strain (differences between *out-of-* and *in-plane* Cauchy strain from 2.3×10^{-3} to -15.5×10^{-3}) are grown on MgO(001). The influence of strain and shape anisotropy on PMA are investigated for each sample and it is found that the shape is the most significant factor of PMA in each case. In addition, the strain component is found to have a significant contribution, which is 11% to 63% the size of the shape contribution, in each case. The focus on shape anisotropy leads to the consideration of two terms of shape anisotropy. Among these samples, the first term of the shape anisotropy, which is due to the energy of a single magnetic dipole, is responsible for an effect ranging only 5% to 6% the size of the total PMA. On the other hand, in these thin films a second order

(dipole-dipole) term of shape anisotropy is found to be the most significant component of PMA. It is predicted that this second shape term is a significant component of PMA in films with t up to $\sim$360 nm. This second shape term is found to be primarily due to the energy inherent in a shape attributed to dipole-dipole interaction, which is mediated by the internal (molecular) magnetic fields produced by opposing Ising domains.

2. Procedure

All sample growths were performed in a custom designed ultra-high vacuum molecular beam epitaxy system.[32] Thin samples (#1 and #2), which were 310 ± 33 nm and 106 ± 12 nm thick respectively, were grown with the method outlined for high-purity ε-Mn_4N on MgO(001) growth in our previous work.[6] One or more annealing step(s) using a substrate temperature of 772 °C were used in addition to the previous method on the ultrathin samples (#3 and #4), which were each 9 ± 1 nm thick.

Reflection high-energy diffraction (RHEED) is actively used *in-situ* with a 20 keV incident electron beam energy in order to monitor surface structure as well as the lattice values parallel to the sample plane during growth. Lattice measurements based on the RHEED streak spacings are calibrated using the post-annealing MgO substrate streak spacings as a reference for each growth. *Out-of-plane* x-ray diffraction (XRD) measurements are taken *ex-situ* using Cu K_α x-rays in order to determine the bulk crystal structure and the lattice values normal to the sample plane. A growth rate calibration is performed using Rutherford backscattering spectrometry (RBS) to determine Mn flux from the Mn deposition over time for one test sample. The thicknesses of samples #1 and #2 are known by using the same growth rate as the test sample for different known times. On the other hand, the thicknesses of #3 and #4 are determined individually using separate RBS measurements so that any Mn lost during annealing step(s) is accounted for.

Vibrating sample magnetometry (VSM) and superconducting quantum interference device (SQUID) measurements are performed on the thin and ultrathin films, respectively, in order to determine magnetic hysteresis, as well as the anisotropic magnetic field (H_K) and saturation magnetization (M_S). The diamagnetic signal from the MgO substrate is subtracted from the VSM or SQUID measurement for each sample using the VSM measurement of a blank MgO substrate as a reference.

Atomic (magnetic) force microscopy is performed using a Park Scientific CP AFM/MFM head retrofitted with a new controller system by Anfatec Inc., which is operated *ex-situ* to obtain information about the topographical and magnetic properties of the sample. The magnetic polarization states in proximity to the surface of the samples are measured using MFM in a method similar to that of Park *et al.*[33] The magnetic polarization ($P = \frac{N_\uparrow - N_\downarrow}{N_\uparrow + N_\downarrow}$) is determined for each sample by using the distributions of the magnetic contrast in MFM images of each sample as an approximation of the distribution of magnetization states in

the sample. These distributions of magnetic contrast are normalized to the range of the distribution. Then, the relative number of states in the distribution above compared to below zero magnetic polarization is found and used to calculate $P = \frac{N_\uparrow - N_\downarrow}{N_\uparrow + N_\downarrow}$. A Fisher Scientifc FS60 Ultrasonic Cleaner was used to vibrate the samples for ~ 10 min intervals in order to remove any net magnetic polarization in the samples.

3. Results and Discussion

3.1. Ultrathin ε-Mn_4N Growth and Strain Control

The steps of growth, which involve annealing and regrowth, for samples (#3 and #4) can be followed in Fig. 1. The first two steps follow the method of our previous work by annealing an MgO(001) substrate [RHEED image shown in Fig. 1(a)] and then depositing a Mn_xN_y thin film [RHEED image shown in Fig. 1(b)].[6] Thirdly, the sample is annealed at 772 °C, which is found to remove Mn_xN_y material from the sample while at the same time the Mn_xN_y is annealed towards a higher phase purity of ε-Mn_4N.

In the initial growth (first step) of samples #3 and #4, some undetermined Mn_xN_y phase and/or mix of Mn_xN_y phases, which cannot be identified from RHEED (the only *in-situ* measurement available), are grown. Removal of some of the Mn_xN_y material is confirmed in RBS measurements, which find the finished samples to be thinner than expected based on the known Mn flux and total time of growth.

Among the phases of the Mn_xN_y system, 2× streaks are the unique signature for ε-Mn_4N.[18] Therefore, an increase in ε-Mn_4N phase purity is observed in the appearance of 2× streaks in Fig. 1(c) after an annealing step (second step) when there were previously no 2× streaks as in Fig. 1(b). Annealing from Mn_xN_y to ε-Mn_4N is in agreement with the observation of Suzuki *et al.*, in which the tetragonal phases of the Mn_xN_y system could all be annealed into ε-Mn_4N.[34]

The second step (annealing) is concluded just as inner first order streaks (4.21 Å) begin to reappear alongside the outer first order Mn_xN_y streaks (3.93 Å) along the MgO[100] direction as seen in Fig. 1(c). The spacing of the inner first order streaks matches the streak spacing of MgO[100].[18] The outer first order streaks (3.93 Å) in Fig. 1(c) are identified as ε-Mn_4N streaks because of the signature 2× streaks corresponding to them.

In the third step (regrowth), high phase purity ε-Mn_4N is deposited to the desired t on what is expected to be a mostly ε-Mn_4N template at 641°C for samples #3 and #4. High temperature annealing of Mn_xN_y thin films has the potential to introduce ζ-phase grains into the samples.[6] However, the high ε-Mn_4N phase purity of each finished sample (#1 through #4) is confirmed through the three methods established in our previous work; namely, a single set of 1st order streaks with corresponding bright 2× streaks along MgO[100] in RHEED as seen in Fig. 1(d), the presence of only the ε-Mn_4N peak among the known MgO substrate peaks (and no other significant peaks such as ζ peaks) in

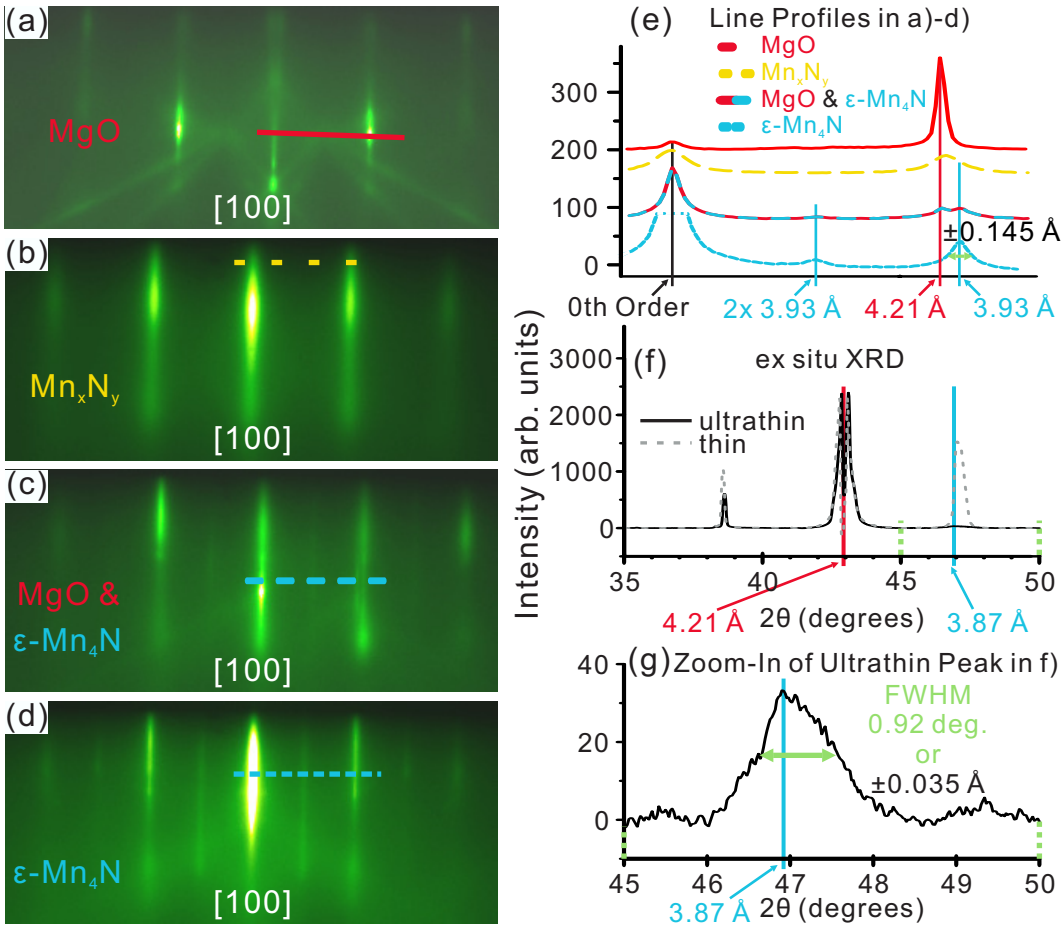

Figure 1: RHEED images taken along MgO[100] of (a) an MgO substrate before any deposition, (b) initially grown Mn_xN_y material, (c) an ultrathin ε-Mn_4N sample after annealing, and (d) a ultrathin sample after regrowth. (e) Line profiles across the RHEED patterns in a) to c). (f) *ex-situ* XRD of an ultrathin sample. (g) Zoom-in of the ε-Mn_4N(002) peak in f).

XRD as seen in Figs. 1(f)/(g), and the presence of a single uniform morphology with magnetic contrast throughout in AFM/MFM images.[6]

In a previous study, if Mn_xN_y grains other than ε-Mn_4N were grown in the nucleation step, these Mn_xN_y grains would continue to grow alongside ε-Mn_4N grains when growth conditions favored ε-Mn_4N phase purity.[6] Therefore, it is expected that if the ultrathin samples (#3 and #4) are grown on a template, which has Mn_xN_y phase grains alongside ε-Mn_4N grains, then Mn_xN_y grains would be present throughout the sample. However, the ε-Mn_4N phase purity of the samples has been confirmed by RHEED, XRD and AFM/MFM measurements, which show that Mn_xN_y phase grains are not present throughout the sample. Hence, due to the high ε-Mn_4N phase purity of the final growths together with the clear 2× signature and dim 4.21 Å (spacing in agreement with MgO) streaks in Fig. 1(c), only ε-Mn_4N and to a lesser extent MgO are expected to be present following the annealing step (second).

Before the second step (annealing), the sample is composed of a mix of phases (such as η-Mn_3N_2 and ε-Mn_4N). These mixed phase samples are known to have lattice constants larger than pure ε-Mn_4N samples because of the larger lattices of the other phases, such as η-Mn_3N_2 ($a = 4.21$ Å and $c/3 = 4.03$ Å), compared to ε-Mn_4N (3.86 Å) leading to a net increase in lattice values.[6] As observed by Suzuki *et al.*, annealing can be used to obtain ε-Mn_4N from Mn_xN_y phases with lower Mn:N ratios.[34]

In this study, it is found that repetition of the second and third steps (annealing and regrowth) sequentially reduces the lattice values of the sample towards the unstrained lattice value of ε-Mn_4N (3.86 Å) after starting with the larger lattice of a mixed phase sample. Therefore, if the lattice value(s) observed with RHEED following the third step (regrowth) are larger than those desired, the second and third steps (annealing and regrowth) can be repeated until the desired lattice value(s) are reached. For example, sample #4 underwent a greater number of annealing steps than sample #3 and as a result sample #4 has less strain compared to sample #3 as shown in Table 1. This strain reduction may be related to an increase in crystal dislocations due to additional regrowth steps.

In this study, the range of lattice constants of high-purity ε-Mn_4N samples grown without annealing step(s) are from 3.85−3.88 Å. This range roughly agrees with the ranges found in other investigations.[19, 29] The method in this study, which uses annealing step(s) in the growth of ultrathin samples (#3 and #4), had the benefit of increasing the upper limit of the range of the *in-plane* and *out-of-plane* lattice constants to 3.93 and 3.87 Å respectively. The larger lattice constants are confirmed using *in-plane* RHEED measurements as seen in the line profiles in Fig. 1(e) and *out-of-plane* XRD as seen in Fig. 1(g). In this way, the use of annealing step(s) allowed this study to investigate the influence of lattice values on the magnetic properties of ε-Mn_4N over a wider range than previously available.

3.2. Observation of an Additional Component of Out-of-Plane Anisotropy

The total uniaxial anisotropy energy (E_A) of each sample is calculated from the magnetization versus $\vec{\mathbf{H}}$-field measurements (VSM/SQUID). E_A cor-

responds to the energy difference between magnetizing a sample under two different field directions. For this study, this energy difference corresponds to the area between the curves (*in-* and *out-of-plane* $\vec{\mathbf{H}}$-field) seen in Figs. 2(a) through (d) for each individual sample. The area is approximated using the well known triangle approximation ($E_A = M_S H_K/2$). The triangle approximation treats the area between the *in-* and *out-of-plane* curves as a right triangle with catheti equal to the saturation magnetization (M_S) and anisotropic field (H_K). M_S is the maximum magnetic polarization of the sample. H_K is the minimum field magnitude at which both the *in-* and *out-of-plane* $\vec{\mathbf{M}}$-$\vec{\mathbf{H}}$ curves intersect at M_S. The (M_S,H_K) points for the samples are extrapolated from the $\vec{\mathbf{M}}$-$\vec{\mathbf{H}}$ curves and are shown as squares on the ends of the extrapolated lines (dotted) in Fig. 2 for samples #1 to #4.

In all four samples, a smaller $\vec{\mathbf{H}}$-field is needed to fully magnetize the samples *out-of-plane* than to magnetize them *in-plane* as seen in Fig. 2. This favorability to *out-of -plane* magnetization over *in-plane* means the samples all possess *out-of-plane* PMA. In addition, a large area, which means a large anisotropy energy, is present between the $\vec{\mathbf{M}}$-$\vec{\mathbf{H}}$ curves for all four samples as seen in Fig. 2. Therefore, each sample has a large *out-of-plane* PMA.

A much larger M_S is found for sample #4 (195 ± 24 $\frac{emu}{cm^3}$) compared to the other three samples (120 ± 12, 122 ± 13, and 127 ± 13 $\frac{emu}{cm^3}$). This higher M_S may be due to a larger shape component for the ultrathin samples combined with sample #4 having a much smaller magnitude of tetragonal strain [$(-2.6 \pm 2.6) \times 10^{-3} = -\frac{a-c}{a_0}$] compared to the other ultrathin sample [$(-15.5 \pm 2.6) \times 10^{-3} = -\frac{a-c}{a_0}$] as seen in Table 1. An elevated M_S (145 $\frac{emu}{cm^3}$) was seen by Yasutomi *et al.* in samples a little thicker (12 to 28 nm) and with a little more tetragonal strain ($-\frac{a-c}{a_0} = -5.2 \times 10^{-3}$ to -10.4×10^{-3}) than sample #4.[19]

Strangled hystereses such as that seen in the *out-of-plane* SQUID measurements of the ultrathin samples in Figs. 2(c) and (d) are associated with samples composed of separate regions, which possess different ferromagnetic (or in this case ferrimagnetic) structures (for example regions with different M_S, coercivity, ...).[35] Significant incorporation of ζ-phase, which has been found to possess ferromagnetic properties that differ from ε-phase, is ruled out due to a lack of corresponding XRD peaks as shown in Fig. 1(f).[36] However, experimental and theoretical evidence has shown that lattice parameters influence the magnetic properties (M_S and coercivity) of ε-Mn_4N.[14, 16, 28, 29, 30, 31] Therefore, it is reasonable to conclude that regions with different ferrimagnetism (M_S and coercivity) exist in the ultrathin samples because of the wide variation of lattice parameters found in the ultrathin samples (#3 and #4) as seen in the full width half maximum (FWHM) from the RHEED (0.29 Å) in Fig. 1(e) and of the XRD (0.07 Å) in Fig. 1(g).

The angle of the easy-axis with respect to the sample surface normal (Θ) can be calculated from the remnant magnetization (M_r) when a field is applied perpendicular and parallel to the sample surface: $\Theta = tan^{-1}(\frac{M_{r\parallel}}{M_{r\perp}})$.[37] This calculation gives easy-axis angles of $8^\circ = tan^{-1}(\frac{15\ \frac{emu}{cc}}{109\ \frac{emu}{cc}})$, $5^\circ = tan^{-1}(\frac{10\ \frac{emu}{cc}}{116\ \frac{emu}{cc}})$,

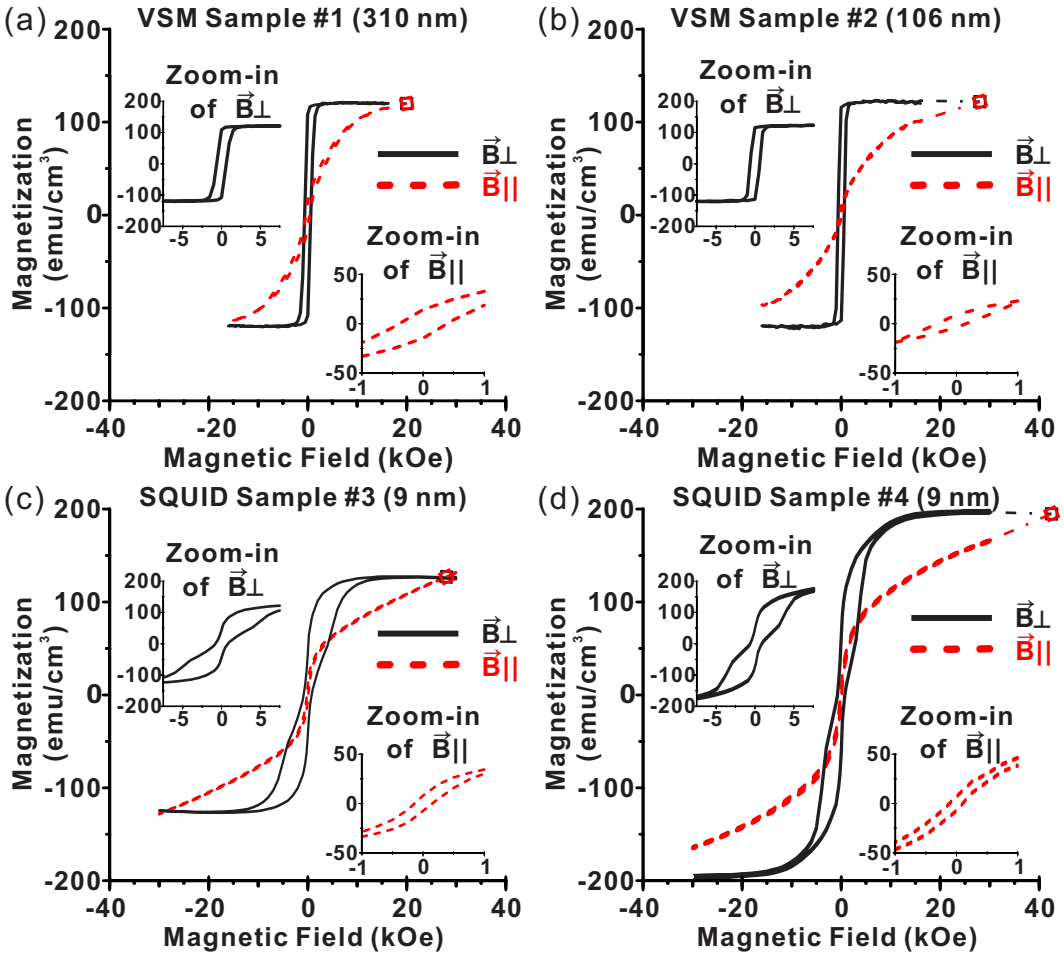

Figure 2: Two RT VSM and two RT SQUID taken of the ε-Mn_4N samples ((a) #1, (b) #2, (c) #3 and (d) #4) with the applied $\vec{H}$-field parallel (dotted) and perpendicular (solid) to [100]. Dotted lines and squares illustrate the extrapolated magnetic polarization curves and the point (H_K, M_S), respectively, for each sample.

Sample	Thickness t (nm)	Strain Coefficient $-\frac{a-c}{a_0}$ (10^{-3})	Surface Polarization P_S (%)	Saturation Magnetization M_S $(\frac{emu}{cm^3})$	Anisotropy Field H_K (kOe)
#1	310 ± 33	2.3 ± 2.3	22 ± 1	120 ± 12	20.0 ± 0.5
#2	106 ± 12	-5.4 ± 2.6	37 ± 3	122 ± 13	28.0 ± 0.5
#3	9 ± 1	-15.5 ± 2.6	78 ± 3	127 ± 13	28.0 ± 0.5
#4	9 ± 1	-2.6 ± 2.6	82 ± 3	195 ± 24	42.5 ± 0.5
Sample	Anisotropy Energy E_A $(\frac{Merg}{cm^3})$	Strain Anisotropy K^V $(\frac{Merg}{cm^3})$	Single-Dipole Shape Anisotropy K^{S_1} $(\frac{Merg}{cm^3})$	Dipole-Dipole Shape Anisotropy K^{S_2} $(\frac{Merg}{cm^3})$	Relative Size of Dipole-Dipole Term $\frac{\lvert K^{S_2}\rvert}{\lvert K^V\rvert+\lvert K^{S_1}\rvert+\lvert K^{S_2}\rvert}$ (%)
#1	1.2 ± 0.1	0.4 ± 0.3	-0.09 ± 0.01	0.8 ± 0.3	62
#2	1.7 ± 0.2	-1.1 ± 0.4	-0.09 ± 0.01	2.9 ± 0.5	71
#3	1.8 ± 0.2	-3.0 ± 1.0	-0.10 ± 0.01	4.9 ± 1.0	61
#4	4.1 ± 0.5	-0.5 ± 0.3	-0.24 ± 0.03	4.9 ± 0.6	87

Table 1: The first five rows show the thickness, strain coefficient, surface polarization, saturation magnetization and anisotropy field for each sample. These values are found from RBS, RHEED/XRD, MFM distributions, VSM(samples #1 and #2)/SQUID(samples #3 and #4) and VSM(samples #1 and #2)/SQUID(samples #3 and #4) respectively. The second five rows show the anisotropy energy, each individual component of the anisotropy energy and the relative size of the dipole-dipole term. These values are calculated from the data in the first five rows.

$13^\circ = tan^{-1}(\frac{10\ \frac{emu}{cc}}{44\ \frac{emu}{cc}})$, and $7^\circ = tan^{-1}(\frac{8\ \frac{emu}{cc}}{63\ \frac{emu}{cc}})$ for samples #1, #2, #3, and #4 respectively. In all cases, the easy-axis has a large *out-of-plane* component (more than 4 times larger than the *in-plane* component), which is a useful property for a spin-injection contact.[22] Both ultrathin samples (#3 and #4) have smaller $M_{r\perp}$ than the thin samples (#1 and #2) due to the lower slope ($\mathbf{M}$ vs $\vec{\mathbf{H}}_\perp$) related to the strangled shape of the hysteresis loops of samples #3 and #4.

The energy difference between the curves (E_A) is expected to be the sum of various individual components with each individual component caused by separate phenomena. It is proposed by Yasutomi *et al.* that E_A in ε-$Mn_4N(001)$ films with t significantly greater than a few nanometers ($3-5$ nm) can be calculated from the sum of the strain and shape components (K^V and $K^{S_1} = -2\pi M_S^2$ respectively):

$$K^V = -\frac{3}{2}\lambda_{100}(C_{11}-C_{12})(\frac{a-c}{a_0}), \tag{1}$$

where λ_{100} is the magnetostriction constant along [100], C_{11} is the elastic modulus perpendicular to the surface, C_{12} is the elastic modulus parallel to the surface and λ_{100} is known to be negative.[15, 17, 19]

The *in-plane* lattice values are calculated from *in-situ* measurements of the RHEED streak spacings of the samples using the post-annealing RHEED patterns of the MgO substrates as a reference. The *out-of-plane* lattice values are calculated from the XRD measurements of the samples using the MgO 002 peak as a reference. The value for a_0 is taken from the accepted literature value of 3.86 Å.[12]

Samples #3 to #4 are found to have the same thickness and similar shape. Therefore, the main difference, which is relevant to the E_A of the samples, between samples #3 to #4 is that sample #3 has a substantially larger tetragonal strain compared to sample #4. Due to this, the difference between the E_A of samples #3 to #4 should be almost completely due to strain after accounting for K^{S_1} (small differences in shape). Any differences due to thickness should be minimal because the samples have the same thickness (9 ± 1 nm). Therefore, $\frac{3}{2}\lambda_{100}(C_{11}-C_{12})$ is calculated using the values shown in Table 1 as follows:

$$K^V_{\#3} - K^V_{\#4} \cong E_{A_{\#3}} - E_{A_{\#4}} - (-2\pi(M_{S_{\#3}} - M_{S_{\#4}})) \tag{2}$$

and after inserting Eq. 2 into Eq. 1

$$\frac{3}{2}\lambda_{100}(C_{11}-C_{12}) \cong \frac{K^V_{\#3} - K^V_{\#4}}{(-\frac{a_{\#3}-c_{\#3}}{a_0}) - (-\frac{a_{\#4}-c_{\#4}}{a_0})}. \tag{3}$$

This gives a positive value for $\frac{3}{2}\lambda_{100}(C_{11}-C_{12})$ ($= 193 \pm 60\frac{Merg}{cm^3}$). A positive $\frac{3}{2}\lambda_{100}(C_{11}-C_{12})$ and a negative λ_{100} means that $C_{11} < C_{12}$ and K^V is negative when $a > c$. A $C_{11} < C_{12}$ is unusual in comparison to many other cubic materials and anti-perovskite nitrides.[19, 38, 39]

The strain components are calculated using the value for $\frac{3}{2}\lambda_{100}(C_{11}-C_{12})$ and are shown in Table 1. Samples #2 to #4 all have large positive E_A (> 1

$\frac{Merg}{cm^3}$) despite having negative contributions from both the strain (K^V) and shape due to single dipole (K^{S_1}) components. In addition, after accounting for the K^V and K^{S_1} components there remains an additional large and *out-of-plane* anisotropy (circles) seen in Fig. 6(a). This additional anisotropy energy shows a negative linear relationship with t. From this, the presence of an additional component of E_A (K^{S_2}), which is large, positive (*out-of-plane*), and varies proportionally with $-t$ for $t = 9$ to 310 nm is found.

3.3. Observation Of an Out-Of-Plane Separation Of Magnetically Opposing Regions

AFM images of the surface morphology of the thin samples (#1 and #2) are seen in Figs. 3(a) and (b). The morphology of samples #1 and #2 consists of flat square-shaped terraces. The MFM images of the thin samples when at zero net magnetic polarization, which correspond to the areas seen in Figs. 3(a) and (b), are seen in Figs. 3(c) and (d) respectively. The magnetic domains of samples #1 and #2 are arranged in semi-continuous paths. The morphology and magnetic domain structure seen in Fig. 3 are consistent with the morphology and magnetic domain structure, which were observed in thin films composed of single-phase ε-Mn_4N as detailed in our previous work.[6]

AFM images of the surface morphology of the ultrathin samples (#3 and #4) are seen in Figs. 4(a) and (b). The morphology of samples #3 and #4 consists of box canyon-shaped valleys and mesa-like islands. The box canyon-shaped valleys are separated from one another and contain multiple isolated islands, which have widths generally 0.1 to 0.2 μm across and heights generally 1 to 6 nm tall. In contrast, the mesa-like islands are interconnected, possess a larger range of widths (0.1 to 1 μm across) and taller heights (7 to 10 nm).

The mesa-like island heights are in some cases taller than the t of the corresponding sample because t is the average thickness and does not account for surface morphology. Using AFM measurements, samples #3 and #4 are found to typically have islands 7 nm and 10 nm tall, which cover $52 \pm 5\%$ and $54 \pm 5\%$ of the surface, respectively. The thickness of the base layer of each sample is calculated by subtracting out the contribution of the islands to the total thickness (t), which gives 5.5 nm = 9 nm − (52% × 7 nm) and 3.5 nm = 9 nm − (54% × 10 nm) thick base layers for samples #3 and #4 respectively.

The MFM images of the ultrathin samples when at zero net magnetic polarization, which correspond to the areas seen in Figs. 4(a) and (b), are shown in Figs. 4(c) and (d) respectively. The areas over the mesa-like islands are found to generally have an opposing magnetic polarization to the box canyon-shaped valleys. This difference in polarization indicates the magnetic polarization at the surface depends on surface height in the ultrathin samples.

Using our variation of the Park *et. al* technique, the magnetization measurements, which correspond to the individual pixels within the MFM image of each sample, are assembled into a distribution for each sample as seen in Fig. 5. The distributions in Figs. 5(a) and (b) are the distributions of magnetic states in samples #1 and #2, respectively, over the whole morphology in the image areas. The distributions in Figs. 5(c) and (d) are the distribution of magnetic

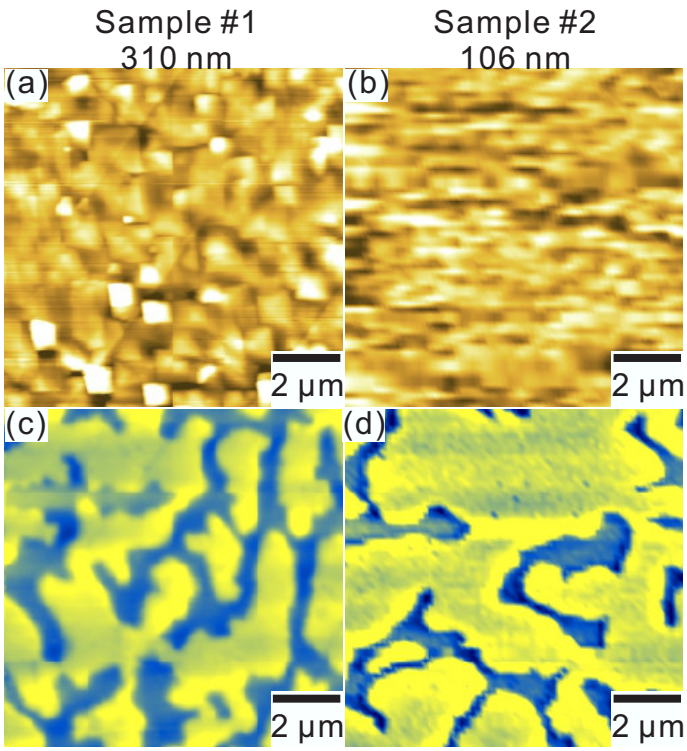

Figure 3: AFM/MFM images of the thin samples #1 (310 nm) and #2 (106 nm). (a) and (b) each show a 10 μm AFM topographic image of the samples #1 and #2 respectively. (c) and (d) each show a 10 μm MFM image, which are taken when each sample is demagnetized and correspond to the same area shown in a) and b) respectively.

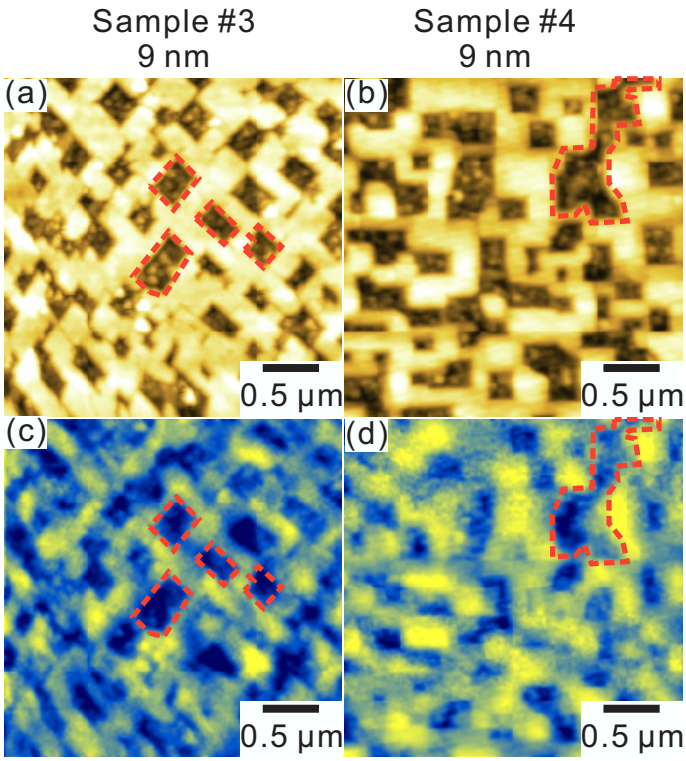

Figure 4: AFM/MFM images of the ultrathin samples #3 (9 nm) and #4 (9 nm). (a) and (b) each show a 3 μm AFM topographic image of the samples #3 and #4 respectively. (c) and (d) each show a 3 μm MFM image, which are taken when each sample is demagnetized and correspond to the same area shown in a) and b) respectively. Dotted lines around box canyon-shaped valleys in a) and b) are mapped onto c) and d) to illustrate the dark magnetic contrast commonly associated with these areas.

states in samples #3 and #4, respectively, over the whole morphology in the image areas (squares) and over only the mesa-like islands (circles).

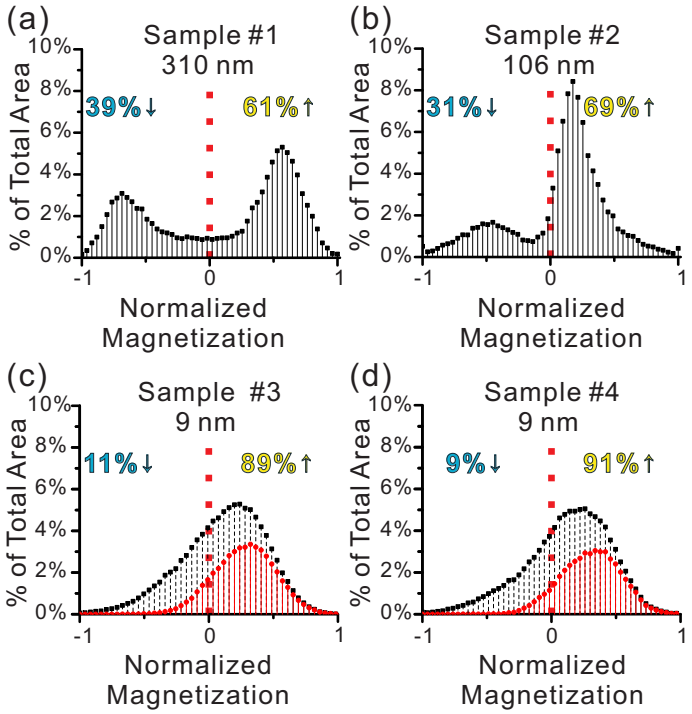

Figure 5: The distribution of the surface magnetization of each sample when the sample is demagnetized: (a) #1 (310 nm thick), (b) #2 (106 nm thick), (c) #3 (9 nm thick), and (d) #4 (9 nm thick). The distributions in c) and d) show the unit area magnetic polarizations (squares) of the complete area and the unit area magnetic polarizations (circles) of only the island areas.

A non-zero local magnetic polarization (P_S) is found in each of the samples when the samples have net zero magnetization as seen in the higher spin-up populations ($N_\uparrow > N_\downarrow$) in Fig. 5. The MFM data in Figs. 3(c) and (d) shows no correlation to the topography of the thin samples (#1 and #2); namely, the flat square terrace morphology seen in Figs. 3(a) and (b). On the other hand, a clear correlation between polarization and topography is observed as film thickness drops below ∼15 nm (samples #3 and #4). Due to the correlation between surface height and magnetic polarization, the state distributions [Fig. 5(c) and (d)] taken using the area above the mesa-like islands (solid) are used to determine the magnetic polarization near to the surface for these samples.

The non-zero local magnetic polarization measured from above the surface of the samples, which overall have zero magnetic polarization, is explained by the observed polarization near the surface being canceled out by an equal and opposite polarization further from the surface. This separation in polarization near and away from the sample surface can be explained by partially overlap-

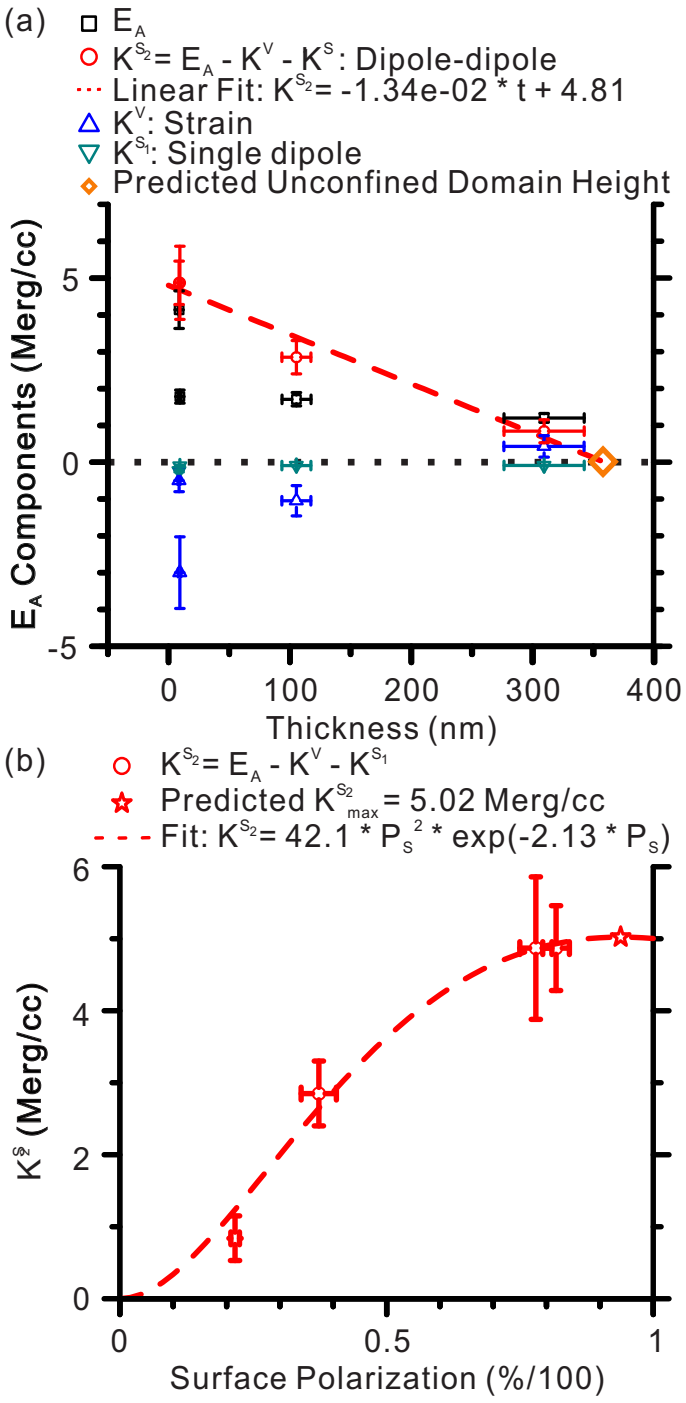

Figure 6: (a) Plot of thickness (t) versus the anisotropy energy (E_A) and each of the components of E_A. The linear model for a second term of the shape component (K^{S_2}) is denoted by the red rounded dashed line. The zero energy level is marked with the black dashed square line. (b) Plot of surface polarization (P_S) versus change in K^{S_2}. The red rounded dashed line marks the $K^{S_2} \cong DP_S^2\, e^{-bP_S}$ model fit. See Table 1 for a full list of these values and corresponding errors.

ping magnetic domains. A feature, which is predicted by partially overlapping magnetic domains, is that the magnitude of the magnetic signal in an MFM image would vary across single domains at the surface depending on whether an opposing domain lies beneath. Such a varied signal is observed for samples #1 and #2 in Figs. 3(c) and (d), in which different regions within individual magnetic domains appear brighter and darker. As well, a varied signal can be observed across the mesa-like islands in Figs. 4(c) and (d), in which the signal over the mesa-like islands goes from brighter to darker without transitioning to a fully dark signal, for samples #3 and #4 respectively.

In the case of the thin samples (#1 and #2), a decrease in the separation of the $N_{\uparrow}$ and $N_{\downarrow}$ peaks in the magnetic polarization distributions can be seen when comparing Fig. 5(a) to Fig. 5(b). The peak separation in Fig. 5(b) decreases for the thinner and more polarized sample (106 nm and 37%) when compared to the peak separation in Fig. 5(a) of the thicker and less polarized sample (310 nm and 22%). This decrease in peak separation can be explained by the opposing domains below the surface masking some of the signal coming from the domains near the surface. This masking would be expected to be greater in the thinner and more polarized sample (#2) because the anticipated opposing domains, which lie beneath much of the surface domains, would be closer to the point of measurement (above the surface) and occupy a larger area under the surface domains. In the case of the ultrathin samples (#3 and #4), a significant portion of opposing polarization must be below the surface because the polarizations observed across the entire morphology of the samples, 26±1% and 40±1%, are both positive as seen in Figs. 5(c) and (d) for samples #3 and #4 respectively.

Previously, the domain structure in this system was identified to consist of "pancake-like" Ising domains with magnetic force microscopy.[6] Ising domains partially overlapping *out-of-plane* serves as an explanation of the previous identification of an Ising domain structure as well as the MFM evidence, which is presented in this study, of magnetic polarization near the surface in these demagnetized samples. Not dissimilar to ε-Mn_4N, Ising domains with a "pancake-like" shape, a large uniaxial anisotropy, and *out-of-plane* packing have been observed in single crystal $LuFe_2O_4$ (also a ferrimagnet) by Wu *et al.*[40]

3.4. Energy of the Dipole-Dipole Interaction

After considering the MFM evidence, samples #1 through #4 are each found to contain adjacent opposing dipoles, which have *out-of-plane* overlap, while demagnetized and under zero external field. Therefore, a model of the system energy of these samples should consider the energy associated with the local magnetic polarization due to this *out-of-plane* overlap when the sample is demagnetized and there is no external field. The component of the system energy related to the magnetization of a material when there is no externally applied field is given by:

$$E \propto MB = M\lambda M \propto M^2; \tag{4}$$

where λM is the molecular (internal) field and λ is the Curie temperature divided by the Curie constant.[41]

The Brillouin expression for magnetization, which includes the effect of a dipole-dipole interaction (multiplying by the hyperbolic tangent shown below) when no external magnetic field is applied, is as follows:

$$M = N\mu \tanh(\frac{\mu^2 \lambda N}{k_B T}), \tag{5}$$

where μ is the magnetization of a single unit cell, $N = N_\uparrow - N_\downarrow$ is the net number of unit cells magnetized, T is the temperature, and $\mu^2\lambda N/k_B = T_C$ is the Curie temperature.

When $(T_C \cong 738K) \gg (T \cong 298K)$, the approximation:

$$\tanh(N\xi) \cong 1 - 2e^{-2N\xi} ..., \tag{6}$$

where $\xi = \mu^2\lambda/k_B T$, is valid.[12, 41] In addition, $N \propto P_S$. Therefore,

$$\Delta M = M(0) - M(P_S) \cong aP_S(-1 + 2e^{-bP_S}...) \tag{7}$$

and from inserting Eq. 7 into the change in E from Eq. 4,

$$\Delta E \propto M\Delta M \cong -CP_S^2 \ + \ DP_S^2 \, e^{-bP_S} ..., \tag{8}$$

where a, b, C, and D are constants.

The first term in Eq. 8 ($\propto -P_S^2$) matches the energy of a single magnetized dipole (i.e. the hyperbolic tangent in Eq. 5 is equal to 1) and is proportional to the square of the net magnetization of the entire sample. In the considered case (a demagnetized sample under no externally applied field) the sample has zero net magnetization. Therefore, the first term in Eq. 8 ($\propto -P_S^2$) is expected to go to zero. It should be noted, when the sample is at M_S the first term is non-zero and corresponds to the first term of shape anisotropy (K^{S_1}). On the other hand, in this case, in which *out-of-plane* Ising domains overlap, a second term,

$$K^{S_2} = DP_S^2 \, e^{-bP_S}, \tag{9}$$

exists due to the consideration of the molecular field interaction between adjacent dipoles (i.e. the hyperbolic tangent in Eq. 5 is not necessarily equal to 1). Therefore, K^{S_2} relates to the stored energy of the molecular field interaction between opposing Ising domains, which overlap *out-of-plane*, in the case of samples #1 through #4.

As seen in Fig. 6(b), there is a strong fit (R-squared 98.5%) between the second term in Eq. 8 due to the molecular field interaction ($\propto P_S^2 \, e^{-bP_S}$) and the additional anisotropy energy term (K^{S_2}), which shows a proportionality to $-t$. Therefore, the second term of Eq. 8 (dipole-dipole) is an energy due to a magnetization, which is attributed to changes in sample shape ($\Delta K^{S_2} \propto -t$). In the same way, the first term of Eq. 8 (single-dipole shape anisotropy) is an energy due to a magnetization, which is attributed to sample shape. This leads to the conclusion that this large positive (*out-of-plane*) PMA term (K^{S_2}) can be attributed to a dipole-dipole interaction associated with a second (dipole-dipole) term of shape anisotropy.

A peak value is observed in the fit of the second term of Eq. 8 with the K^{S_2} data ($K^{S_2} = 42.1P_S^2 e^{-2.13P_S}$) at $(P_S, K^{S_2}) = (94\%, 5.02\ \frac{Merg}{cc})$ as shown in Fig. 6(b). The presence of this peak value predicts a decrease in energy for $P_S > 94\%$. This decrease may be associated with the film approaching the transition to the superparamagnetic limit found in ultrathin ferro/ferrimagnetic films at which point the film would transition towards a single dipole.

The linear behavior of t vs. K^{S_2} can be described by the following model:

$$K^{S_2} = K^{S_2}_{max} - k^{S_2} t, \text{ for } t_0 \leq t \leq t_C \tag{10}$$

where t_0 is the superparamagnetic limit and t_C is the critical thickness at which the domains begin to overlap *out-of-plane*. In this model, K^{S_2} descends away from a maximum value associated with the ideal dipole-dipole polarization as thickness increases.

An increasing area of the domains at the surface as thickness decreases is seen in Figs. 3(c) and (d). Fast Fourier Transforms (FFT) are taken of the magnetic domain maps of samples #1 and #2. These FFT both exhibit a ring-shape. A cross-section through the center of these FFT results in two peaks, and the average of the two widths at 1/e of the maxima provides the range of distances typically found within an image.[42] This analysis of the FFT taken of the domain maps shows typical domain widths of 1.3 μm$> l_d >$ 8 μm and 1.2 μm$> l_d >$ 21 μm for samples #1 and #2 respectively. The maximum of each range is taken to be representative of the domain width of the more common polarization because they are larger at the surface than the domain widths of the less common polarization. Under this convention, a simple calculation of domain volume (V_{ID}) based on the domain area being equal to $\frac{V_{ID}}{t}$ due to Ising domains being bounded by the shape of the sample gives (V_{ID} = Avg. of ((8 μm)$^2 \times$ 310 nm,(21 μm)$^2 \times$ 106 nm) = $\sim$30 μm^3). This $A = \frac{V_{ID}}{t}$ model predicts domain widths of ($\sqrt{\frac{30\ \mu m^3}{9\ nm}}$ =) 58 μm for samples #3 and #4. In agreement, the domains for the ultrathin samples (#3 and #4) continue across the mesa-like islands beyond the range of the scan area of the MFM (>40 μm) (see Supporting Information).

From the observation of increasing domain width with decreasing domain height, it is proposed that when a critical thickness is reached then the Ising domains begin to overlap *out-of-plane* in order to maintain a constant volume. Speculatively, this limit is associated with t reaching the height at which the domain is forced to begin to partially overlap with an adjacent Ising domain in order to reduce the magnetic field external to the sample. Otherwise, the external field would continue to increase as the *in-plane* area of the domains increases with decreasing t in order to maintain a constant domain volume.

Additionally, the need to reduce the external field explains the highly polarized surface of the ultrathin samples (#3 and #4) forming into mesa-like islands (7 to 10 nm in height) as opposed to the less polarized samples (#1 and #2), which form into a flat square terrace morphology. The formation of a highly polarized surface into mesa-like islands allows a direct path for the field lines to reach the oppositely polarized box canyon-shaped valleys. The availability

of a direct path for the field reduces the external field of the sample. When the linear model in Eq. 10 is fit to the K^{S_2} values as seen in Fig. 6, a t of $\sim$360 nm is predicted as the limit at which K^{S_2} goes to zero and the critical t (t_C) at which the domains begin to overlap *out-of-plane*.

The type of domain structure in this study (Ising domains) was determined to result from the pinning of domain boundaries.[33, 40] From the observation of increasing domain width with decreasing domain height, it can be seen that in ε-Mn_4N the domain boundaries are pinned by sample shape. A decrease in microwave absorption with decreasing ε-Mn_4N grain size, which is expected to result from a corresponding decrease in the number of magnetic dipoles, is observed by Yuping *et al.*[23] A likely explanation for this decrease in microwave absorption of ε-Mn_4N is as follows: the decrease in microwave absorption is caused by the number of dipoles, which are not pinned by sample shape, being limited within a particle at grain sizes approaching the volume of a few Ising domains (a few $\sim$30 μm^3).

4. Conclusion

In conclusion, the significant components of PMA in ε-Mn_4N ultrathin/thin films have been accounted for. The scale between the strain component of PMA (K^V) and tetragonal distortion ($-\frac{a-c}{a_0}$) in ε-Mn_4N has been quantified ($\frac{3}{2}\lambda_{100}(C_{11}-C_{12}) = 193 \pm 60\ \frac{Merg}{cm^3}$). The existence of a large positive component of PMA (K^{S_2}), which shows a negative linear relationship with t, is determined. A good agreement between a model for the energy inherent in dipole-dipole overlap *out-of-plane* (due to a second shape term) and the large positive PMA component of ultrathin/thin films of ε-Mn_4N (Eq. 9) is found. As well, the inversely proportional relationship deduced between the area of the domains (A_{ID}) and the sample thickness (t) suggests the previously observed Ising domains in the system roughly maintain a volume of $\sim$30 μm^3 across films of varying t. Further, the negative linear relationship between K^{S_2} and t (Eq. 10) predicts that the previously observed Ising domains in this system begin to overlap *out-of-plane* when the sample thickness drops below a critical thickness ($t_C = \sim 360$ nm) in order to reduce the external field produced by the sample.

In the future, direct measurements of the PMA associated properties (i.e. anomalous hall effect, spin injection efficiency, and microwave absorption) in ε-Mn_4N samples with a range of values for the individual components of PMA would be of interest for determining if/how specific PMA components relate to these associated properties. In addition, whether or not the term K^{S_2} has a significant influence on PMA and the associated properties thereof in ultrathin/thin films of other materials, which contain Ising domains, such as $LuFe_2O_4$ remains to be investigated.

5. Acknowledgements

Research performed at the Ohio University has been supported by the U.S. Department of Energy, Office of Basic Energy Sciences, Division of Materials

Sciences and Engineering under Award # DE-FG02- 06ER46317. Magnetometry measurements performed at the Ohio State University have been supported by the National Science Foundation under Grant # DMR-1507274. A. Foley wishes to thank Andrada-Oana Mandru for useful discussion and Martin Kordesch for the back-coating of substrates as well as useful discussion. Additionally, A.F. wishes to thank Doug Shafer, Todd Koren, Jeremy Dennison and Mike Myers for constructing many of the system components and their help maintaining the system. The authors acknowledge the WSxM software for image processing.[43]

[1] B. Song, J. Jian, H. Bao, H. Li, G. Wang, Y. Xu, X. Chen, Appl. Phys. Lett. **92**, 192511 (2008).

[2] P. Lukashev, R. F. Sabirianov K. Belashchenko, Phys. Rev. B **78**, 184414 (2008).

[3] K. Kamishima, T. Goto, H. Nakagawa, N. Miura, M. Ohashi, N. Mori, T. Sasaki, T. Kanomata, Phys. Rev. B **63**, 024426 (2000).

[4] M.-H. Yu, L. H. Lewis, A. R. Moodenbaugh, J. Appl. Phys. **93**, 10128 (2003).

[5] B. K. Rao, P. Jena, Phys. Rev. Lett. **89**, 185504 (2002).

[6] A. Foley, J. Corbett, A. L. Richard, K. Alam, D. C. Ingram, A. R. Smith, J. Cryst. Growth **446**, 60 (2016).

[7] K. Kabara, M. Tsunoda, J. Appl. Phys. **117**, 17B512 (2015).

[8] C. Li, Y. Yang, L. Lv, H. Huang, Z. Wang, S. Yang, J. Alloys Compd., **457**, 57 (2008).

[9] Y. Wang, W. Y. Liu and Z. W. Fu, Acta Phys.-Chim. Sin. **22**, 65 (2006).

[10] X. Li, Z. Ao, J. Liu, H. Sun, A. I. Rykov, J. Wang, ACS Nano **DOI:10.1021/acsnano.6b07522** (2016).

[11] Y. Au, Q. M. Wang, H. Li, J.-S. M. Lehn, D. V. Shenai, R. G. Gordon, J. Electrochem. Soc. **159**, D382 (2012).

[12] W. J. Takei, R. R. Heikes, G. Shirane, Phys. Rev., **125**, 1893 (1962).

[13] Y. Duan, Q. Xi, Y. Zhang, M. Wen, T. Wang, Appl. Phys. A. **3**, 1075 (2015).

[14] C.-M. Fang, R. S. Koster, W.-F. Li, M. A. van Huis, RSC Adv. **4**, 7885 (2014).

[15] K.M. Ching, W.D. Chang, T.S. Chin, J.G. Duh, H. C. Ku, J. Appl. Phys. **76**, 6582 (1994).

[16] K.M. Ching, W.D. Chang, T.S. Chin, J. Alloys Compd. **222**, 184 (1995).

[17] K.M. Ching, W.D. Chang, T. S. Chin, Appl. Surf. Sci. **92**, 471-471 (1996).

[18] H. Yang, H. Al-Brithen, E. Trifan, D. Ingram, A. R. Smith, J. Appl. Phys. **91**, 1053 (2002).

[19] Y. Yasutomi, K. Ito, T. Sanai, K. Toko, T. Suemasu, J. Appl. Phys. **115**, 17A935 (2014).

[20] S. Nakagawa, Y. Li, M. Naoe, J. Appl. Phys. **81**, 5180 (1997).

[21] S. Dhar, O. Brandt, K. H. Ploog, Appl. Phys. Lett. **86**, 112504 (2005).

[22] N. Ji, M. S. Osofsky, V. Lauter, L. F. Allard, X. Li, K. L. Jensen, H. Ambaye, E. Lara-Curzio, J.-P. Wang, Phys. Rev. B **84**, 245310 (2011).

[23] D. Yuping, H. Gaihua, L. Wei, W. Ming, J. Supercond. Nov. Magn. **29**, 1303 (2016).

[24] X. Shen, A. Chikamatsu, K. Shigematsu, Y. Hirose, T. Fukumura, T. Hasegawa, Appl. Phys. Lett. **105**, 072410 (2014).

[25] M. Meng, S. X. Wu, L. Z. Ren, W. Q. Zhou, Y. J. Wang, G. L. Wang, S. W. Li, Appl. Phys. Lett. **106**, 032407 (2015).

[26] D. Fruchart, D. Givord, P. Convert, P. l′Héritier, J. P. Sénateur, J. Phys. F: Metal Phys. **9**, 2431 (1979).

[27] B. Siberchicot, S. Matar, J. Magn. Magn. Mater. **101**, 419 (1991).

[28] M.S. Miao, A. Herwadkar, W.R.L. Lambrecht, Phys. Rev. B **72**, 033204 (2005).

[29] K. Ito, Y. Yasutomi, K. Kabara, T. Gushi, S. Higashikozono, K. Toko, M. Tsunoda, T. Suemasu, AIP Advances **6**, 056201 (2016).

[30] Y. Imai, Y. Takahashi, T. Kumagai, J. Magn. Magn. Mater. **322**, 2665 (2010).

[31] M. Meinert, J. Phys.-Condens. Mat. **28**, 056006 (2016).

[32] W. Lin, A. Foley, K. Alam, K. Wang, Y. Liu, T. Chen, J. Pak, and A. R. Smith, Rev. Sci. Instrum. **85**, 043702 (2014).

[33] S. Park, Y. Horibe, Y.J. Choi, C.L. Zhang, S.-W. Cheong, Weida Wu, Phys. Rev. B **79**, 180401(R) (2009).

[34] K. Suzuki, T. Kaneko, H. Yoshida, Y. Obi, H. Fujimora, H. Morita, J. Alloys Compd. **306**, 66-71 (2000).

[35] J. Aoki, K. Morii, T. Matsui, Y. Nakayama, Mater. Sci, Eng. B-Adv **10**, L5 (1991).

[36] G.L. Wang, M. Meng, W.Q. Zhou, Y.J. Wang, S.X. Wu, S.W. Li, Mater. Lett. **184**, 291-293 (2016).

[37] K. Wang, E. Lu, J. W. Knepper, F. Yang, A.R. Smith, Appl. Phys. Lett., **98**,162507 (2011).

[38] C. Kittel, Introduction to Solid State Physics, 8th ed. (Wiley, Hoboken, NJ), p. 84.

[39] Z. Wu, J. Meng, Appl. Phys. Lett. **90**, 241901 (2007).

[40] W. Wu, V. Kiryukhin, H.-J. Noh, K.-T. Ko, J.-H. Park, W. Ratcliff II, P.A. Sharma, N. Harrison, Y.J. Choi, Y. Horibe, S. Lee, H.T. Yi, C.L. Zhang, S.-W. Cheong, Phys. Rev. Lett. **101**, 137203 (2008).

[41] C. Kittel, Introduction to Solid State Physics, 8th ed. (Wiley, Hoboken, NJ), p. 326-327.

[42] F. Bai, J. Li, D. Viehland, D. Wu, T. A. Lograsso, J. Appl. Phys. **98**, 023904 (2005).

[43] I. Horcas, R. Fernandez, J. M. Gomez-Rodriguez, J. Colchero, J. Gomez-Herrero and A. M. Baro, Rev. Sci. Instrum. **78**, 013705 (2007).